A MASSIVE MOLECULAR GAS RESERVOIR IN THE $Z = 2.221$ TYPE-2 QUASAR HOST GALAXY SMM J0939+8315 LENSED BY THE RADIO GALAXY 3C220.3

T. K. Daisy Leung and Dominik A. Riechers

Department of Astronomy, Space Sciences Building, Cornell University, Ithaca, NY 14853, USA; tleung@astro.cornell.edu
Draft version July 19, 2015

ABSTRACT

We report the detection of CO($J = 3 \rightarrow 2$) line emission in the strongly-lensed submillimeter galaxy (SMG) SMM J0939+8315 at $z = 2.2212 \pm 0.0001$, using the Combined Array for Research in Millimeter-wave Astronomy (CARMA). The SMG is lensed by the radio galaxy 3C220.3 and its companion galaxy at $z = 0.685$. This measurement allows us to place constraints on the intrinsic properties of the cold gas and dust in the interstellar medium (ISM) of the background SMG which hosts a type-2 quasar, as well as on the spectral energy distribution (SED) of the foreground radio galaxy using the marginally resolved continuum emission detected at an integrated flux density of $S_\nu = 7.5 \pm 1.3$ mJy at 104 GHz. We measure a velocity-integrated CO($J = 3 \rightarrow 2$) line intensity of $I_{\text{CO}(3-2)} = (10.7 \pm 1.3)$ Jy km s^{-1}, corresponding to a lensing- and excitation-corrected CO line luminosity of $L'_{\text{CO}(1-0)} = (2.9 \pm 0.8) \times 10^{10} (10.1/\mu_{\text{L}})$ K km s^{-1} pc^2, where μ_{L} is the lensing magnification factor inferred from our lens modeling of the 1 mm continuum emission. This translates to a molecular gas mass of $M_{\text{gas}} = (2.3 \pm 0.6) \times 10^{10} M_\odot$. We fit optically thick and optically thin modified blackbody models to the SED of the SMG. The preferred optically thick model yields a characteristic dust temperature of $T_{\text{dust}} = 63.1^{+1.1}_{-1.3}$ K in the rest-frame, a dust mass of $M_{\text{dust}} = (5.2 \pm 2.1) \times 10^8 M_\odot$, and a total infrared (IR) luminosity of $L_{\text{IR}} = (9.1 \pm 1.2) \times 10^{12} L_\odot$, after correcting for lensing magnification. We conclude that the intrinsics properties (*e.g.*, gas mass, gas mass fraction, star formation rate) of the molecular gas reservoir in SMM J0939+8315 based on our CO($J = 3 \rightarrow 2$) observations is similar to other high redshift SMGs.

Subject headings: galaxies: formation — galaxies: high-redshift — submillimeter: galaxies

1. INTRODUCTION

Submillimeter-selected galaxies (SMGs) are predominantly found at redshifts $z \sim 1-3$, during the epoch of stellar mass and galaxy assembly, with a tail out to $z > 6$ (Riechers et al. 2013). These galaxies are luminous at submillimeter (submm) wavelengths due to the re-radiation of dust emission peaking at rest-frame far-infrared (FIR) wavelengths (Blain et al. 2002). In the past ~5 years, considerable amounts of effort have been invested into follow-up observations of SMGs that were discovered in large sky surveys (*e.g.*, H-ATLAS, HerMES; Eales et al. 2010; Oliver et al. 2012), conducted using (sub)-mm facilities. These detailed studies have led to growing consensus that SMGs are a population of high-redshift galaxies that are extremely dusty, gas-rich, and luminous ($\gtrsim 10^{12}$ L$_\odot$) at the infrared wavebands, with high star formation rates ($\gtrsim 500$ $M_\odot$yr^{-1}; *e.g.*, Lagache et al. 2005).

To characterize the physical properties of the gas reservoirs in the ISM where active star formation takes place, carbon monoxide (CO) rotational lines have been commonly used as tracers due to its high abundance in the ISM as well as its low excitation energy; the ground state transition line thereby directly probes the cool gas that is essential to fuel star formation (See *e.g.*, Carilli & Walter 2013). Recent observations of CO in SMGs at $z \sim 1-3$ have demonstrated that these galaxies have large gas reservoirs typical of $> 10^{10} M_\odot$(*e.g.*, Riechers et al. 2011a,b; Ivison et al. 2011; Bothwell et al. 2013).

Many recent follow-up observations and thus detailed studies are carried out on SMGs that are gravitationally lensed, as lensing amplifies the intrinsic luminosities of these sources, making them the brightest unveiled in large sky surveys (Negrello et al. 2010; Vieira et al. 2010; Oliver et al. 2012). A particularly interesting, peculiar submm-bright lensing system discovered serendipitously consists of a type-2 quasar host SMG – SMM J0939+8315 (hereafter SMM J0939), lensed by the double-lobed Fanaroff-Riley Class II (FR-II; Fanaroff & Riley 1974) radio galaxy 3C220.3 and its companion galaxy B at $z = 0.685$, where the two lensing galaxies are separated by $1''.5$. SMM J0939 is currently one of the brightest known lensed SMGs, with a lensing-magnified flux density of $S_{250\mu m} = 440 \pm 15$ mJy. Previous detections of CIV 1459Å and HeII 1640Å line emission toward SMM J0939 place the redshift of this galaxy at $z = 2.221$, and suggest the presence of a type-2 quasar, indicating active galactic nucleus activity in this SMG (Haas et al. 2014, hereafter H14).

In this paper, we present the detection of CO($J = 3 \rightarrow 2$) line emission toward the background SMG obtained with the Combined Array for Research in Millimeter Astronomy (CARMA), which refines the redshift, and permits the study of the physical conditions in the ISM of SMM J0939 in great detail. Our measurement of the underlying continuum emission put constraints on the SED of the different components of the foreground FR-II galaxy at mm wavelength (~104 GHz). Based on the magnification factor from our lens model, we infer intrinsic properties of SMM J0939 and thereby conclude this paper by comparing our findings

to other similarly bright, strongly-lensed SMGs at $z \sim 2$.

We adopt a standard ΛCDM cosmological model throughout this paper, with $H_0 = 69.32$ km Mpc^{-1} s^{-1}, $\Omega_M = 0.286$, $\Omega_\Lambda = 0.713$, based on WMAP9 results (Hinshaw et al. 2013). The luminosity distances at $z = 0.685$ and $z = 2.221$ are 4214 Mpc and 19052 Mpc, respectively; $1''$ corresponds to 8.406 kpc at $z = 2.221$, and 7.169 kpc at $z = 0.685$.

2. OBSERVATIONS

2.1. *CARMA*

Observations of the CO($J = 3 \rightarrow 2$) rotational transition ($\nu_{\rm rest} = 345.7959899$ GHz) toward the background galaxy SMM J0939 ($z = 2.221$) were carried out using CARMA at a redshifted frequency of $\nu_{obs} = 107.357$ GHz (2.79 mm) (program ID: cf0142; P.I.: Riechers). The 3 mm receivers were used to cover the redshifted CO($J = 3 \rightarrow 2$) line and the nearby 2.88 mm continuum emission, employing a correlator setup providing a bandwidth of 3.75 GHz in each sideband and a spectral resolution of 5.208 MHz (~ 14.5 km s^{-1}). The line was placed in the upper sideband, with the local oscillator tuned to $\nu_{\rm LO} \sim 104.2609$ GHz. Observations were carried out under good weather conditions in the E array configuration on 2014 July 12. This resulted in 1.56 hours of 15 antenna-equivalent on-source time after discarding unusable visibility data. The nearby source J1039+811 (0.65 Jy) was observed every 20 minutes for pointing, amplitude, and phase calibration. Mars was observed as the primary absolute flux calibrator, and the quasar 3C273 was observed as the secondary flux calibrator. J0927+390 was observed for bandpass calibration, yielding $\sim 15\%$ calibration accuracy. The MIRIAD package was used to calibrate and analyze the visibility data, which are deconvolved and imaged using the CLEAN algorithm with "natural" weighting. This yields a synthesized clean beam size of $11''.3 \times 6''.1$, at a position angle of $-56.1°$ east of north for the upper sideband image cube. The rms noise of the data prior to continuum subtraction is $\sigma_{\rm ch} = 8.75$ mJy beam^{-1} per bin with a channel width of ~ 29 km s^{-1}, whereas the final rms noise of the continuum subtracted data is $\sigma_{\rm ch} = 8.71$ mJy beam^{-1} per bin with the same channel width, and $\sigma = 1.00$ Jy km s^{-1} beam^{-1} over a channel width of 198 MHz (corresponding to ~ 553 km s^{-1}). The continuum image is created by averaging over all line-free channels, this yields a synthesized clean beam size of $11''.9 \times 6''.5$, at a position angle of $-55.9°$ east of north and an rms noise of 0.51 mJy beam^{-1}.

3. RESULTS

3.1. *New Results: 3C220.3*

Averaging over all line-free channels, we detect continuum emission at 9σ significance at an averaged frequency of $\nu_{cont} = 104.2106$ GHz (~ 2.9 mm) in the observed-frame, corresponding to 175.6 GHz (~ 1.7 mm) at $z = 0.685$. In this lens system, the foreground galaxy (3C220.3) is radio-loud, we thus expect the continuum emission to be dominated by the foreground galaxy (see §4.2.1 for details). We use CASA's IMFIT task to estimate the peak position of the continuum emission. The deconvolved source size is $(10''.9 \pm 4''.0) \times (3''.4 \pm 2''.1)$, and the integrated flux density is 7.50 ± 1.30 mJy. At the peak

position of the continuum emission, the peak flux density is $S_\nu = 4.91 \pm 0.54$ mJy beam^{-1}. An overlay image of the 104 GHz continuum emission on the 9 GHz continuum measurement (H14) is shown in Figure 1. This demonstrates that at the resolution of our observations, the continuum emission is marginally resolved. It is therefore plausible that non-thermal emission from both the lobes and the radio core dominate the integrated flux density in our measurement.

The frequency range of our observations covers the HCO$^+$(2−1), HNC($J = 2 \rightarrow 1$), and H$_2$O($3_{13} - 2_{20}$) transition line emission in the foreground galaxy, at the redshifted frequencies of 105.86, 107.71, and 108.79 GHz, respectively. We establish 3σ upper limits employing a typical line width of ~ 300 km s^{-1}, based on the CO($J = 1 \rightarrow 0$) line measurement in the sample of local radio galaxies ($z < 0.1$; Smolčić & Riechers 2011), resulting in 3σ of 7.839 Jy km s^{-1}.

Question for DR: 3sigma using FWHM or total line width (FWZI?)

3.2. *New Results: SMM J0939* *CO($J = 3 \rightarrow 2$) Line Emission*

We detect CO($J = 3 \rightarrow 2$) line emission at $\sim 10(?yes?no?)\sigma$ significance toward the background SMG SMM J0939 at $z = 2.221$. The spatial extent of this SMG is $\sim 5''$, as shown in the Submillimeter Array (SMA) 1 mm dust continuum in Figure 2; as such, the detected CO($J = 3 \rightarrow 2$) line emission is spatially unresolved. The line profile in Figure 2 is therefore extracted at the peak position of the unresolved CO emission. Fitting a four-parameter single Gaussian to the spectrum yields a peak flux density of 21.83 ± 2.68 mJy, superimposed on a continuum level of 4.19 ± 0.49 mJy, and full width at half-maximum (FWHM) of 557 ± 36 km s^{-1}. We construct a velocity-integrated (0th moment) map of the CO($J = 3 \rightarrow 2$) emission from the data after subtracting continuum emission in the visibility plane. This results in a velocity-integrated CO($J = 3 \rightarrow 2$) line flux of $S_{\rm CO} = 10.7 \pm 1.3$ Jy km s^{-1} over the FWZI velocity range of $\Delta v \sim 914$ km s^{-1}, the uncertainty does not include $\sim 15\%$ calibration uncertainty. We ignore primary beam correction given that the source is close to the phase center and is unresolved (*i.e.*, much smaller than the primary beam size). Our CO($J = 3 \rightarrow 2$) line measurement confirms the redshift of SMM J0939, yielding $z = 2.22122 \pm 0.00007$.

4. ANALYSIS

4.1. *Lens Modelling*

To study the intrinsic properties of the background galaxy, we determine the magnification factor by performing lens modeling on the SMA 1 mm archival data of this system. Lens modeling is carried out in the visibility (uv-) plane using the updated version[1] of the publicly available software UVMCMCFIT[2] (Bussmann et al. 2015). The code uses an affine-invariant Markov chain Monte Carlo (MCMC) approach to sample the posterior probability density function (PDF) of the model parameters.
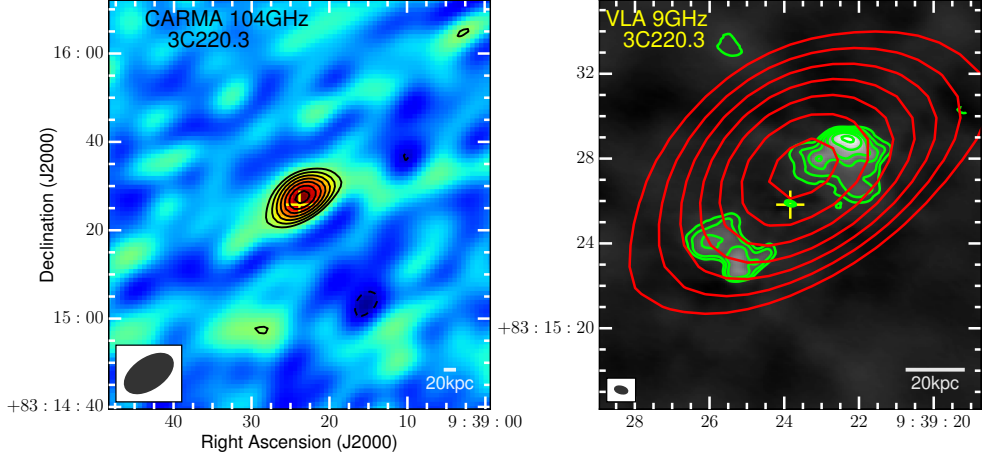
---

[1] commit: 7aee6276
[2] https://github.com/sbussmann/uvmcmcfit

FIG. 1.— Left: Contour map of the 104 GHz continuum emission in 3C220.3. The beam size is $11\rlap{.}{''}9 \times 6\rlap{.}{''}5$, at P.A. $= -56°$, as indicated in the bottom left corner. Right: Contours of the CARMA 104 GHz continuum emission (red) overlaid on the 9 GHz emission (green contours and grayscale; H14). The synthesized beam size of the VLA observations is $0\rlap{.}{''}6 \times 0\rlap{.}{''}2$, at P.A. 76°. The central cross on each image indicates the position of the radio core of 3C220.3. The contour levels of the 104 GHz continuum emission start at $\pm 3\sigma$, incrementing at steps of $\pm 1\sigma$ of 0.5 mJy beam^{-1}; the contour levels of the 9 GHz continuum emission start at $\pm 4\sigma$ where $\sigma = 0.064$ mJy beam^{-1} and increment at steps of $\pm 2^n \sigma$, where n is a positive integer.
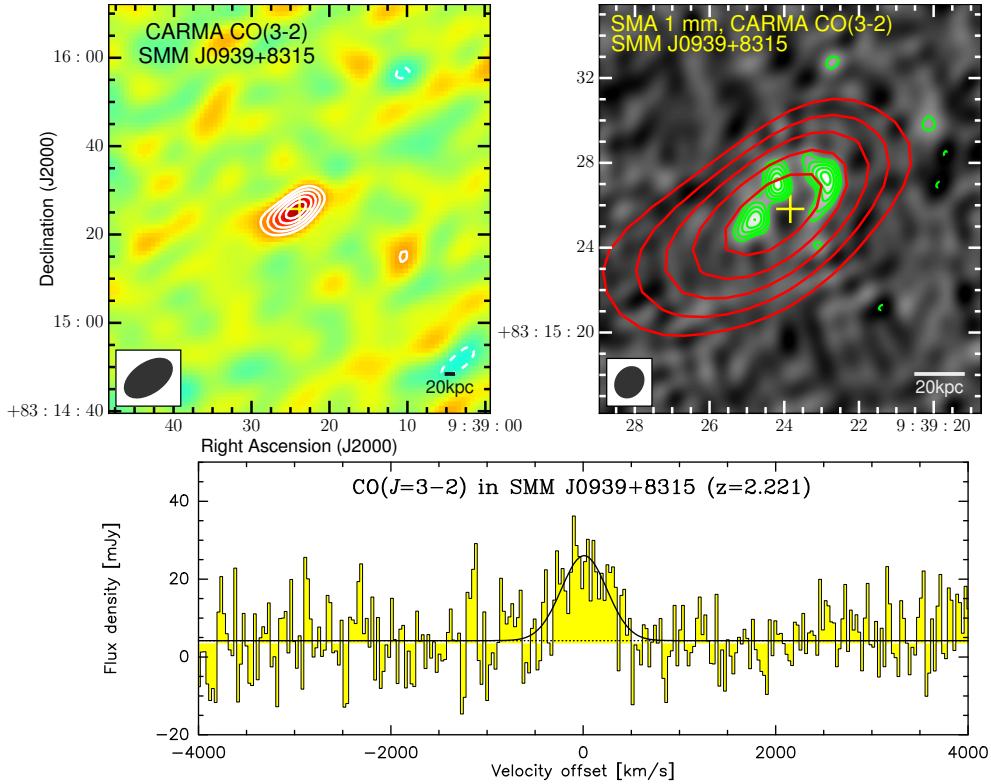

FIG. 2.— Top Left: Continuum-subtracted moment-0 map of CO($J = 3 \rightarrow 2$) line emission toward the background SMG with $\sigma = 1.00$ Jy km s^{-1} beam^{-1} over a velocity range of $\Delta v \sim 553$ km s^{-1}. The angular resolution is $11\rlap{.}{''}3 \times 6\rlap{.}{''}1$, at P.A. $= -56°$, as indicated in the bottom left corner. Top Right: Contours of the CO($J = 3 \rightarrow 2$) line emission (red) overlaid on the SMA 1 mm dust continuum (green contours and grayscale; H14) with $\sigma_{1\,\mathrm{mm}} = 0.84$ mJy beam^{-1}. The beam size of the SMA data is $1\rlap{.}{''}4 \times 1\rlap{.}{''}2$, P.A. $-34°$, as shown in the bottom left corner. The central cross on each image corresponds to the same coordinates as in Figure 1. The contour levels start at $\pm 3\sigma$, incrementing at steps of $\pm 1\sigma$. Bottom: Spectrum extracted at the peak position of CO line emission, with a spectral resolution of $\Delta v \sim 29$ km s^{-1} and an rms of $\sigma_{\mathrm{ch}} = 8.75$ mJy beam^{-1} per channel. Solid black line shows the Gaussian fit to the CO($J = 3 \rightarrow 2$) line profile. Yellow histogram shows the flux density as a function of velocity offset, where the velocity scale is relative to $z = 2.221$.
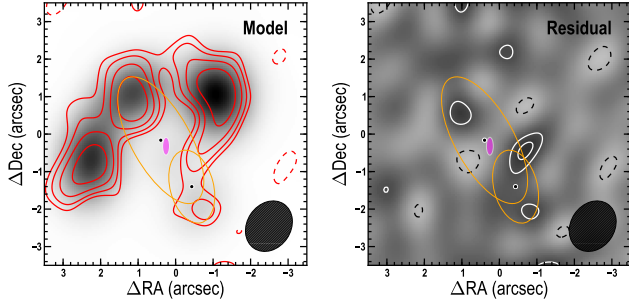
FIG. 3.— Double-lens modeling of SMM J0939 using UVMCMCFIT on the SMA 1 mm continuum data. The contours start at $\pm 2\sigma$, incrementing at steps of $\pm 2\sqrt{2}\sigma$. Solid contours show the positive residuals and dashed contours show the negative residuals. Left: SMA 1 mm continuum (red contours) overlaid on the best-fit model (grayscale image) assuming an elliptical Gaussian profile for the background SMG. The lenses are represented as black dots, the half-light area of the background source is represented as magenta ellipse, and the critical curves are represented as orange curves. Right: Residual contours and image obtained by taking the Fourier transform of the difference between the SMA data and the best-fit model in the visibility plane.

In the code, the surface mass densities of both lenses are represented by singular isothermal ellipsoid (SIE) profiles, and the source is assumed to have an elliptical Gaussian profile. The code does not include an external shear parameter.

We fix the phase center to coordinates (α, δ) (J2000) = (9:39:23.54, 83:15:26.10), the angular offsets of the lenses and source are referenced to this phase center. The primary lens (3C220.3) is described by five free parameters: the angular offset relative to the chosen phase center in the image ($\Delta\alpha_{\mathrm{lens0}}$ and $\Delta\delta_{\mathrm{lens0}}$), the angular Einstein radius (θ_{E0}), the axial ratio (q_{lens0}), and the position angle (ϕ_{lens0}). The secondary lens (companion B) is described by three free parameters: θ_{E1}, q_{lens1}, and ϕ_{lens1}. The angular offset of the secondary lens is sampled with respect to ($\Delta\alpha_{\mathrm{lens0}}$ and $\Delta\delta_{\mathrm{lens0}}$) of the primary lens. The source (SMM J0939) is parameterized by six free parameters: the position of the source relative to the primary lens ($\Delta\alpha_{\mathrm{s}}$ and $\Delta\delta_{\mathrm{s}}$), the total intrinsic flux density (S_ν), the effective radius ($r_{\mathrm{s}} = \sqrt{a_{\mathrm{s}}b_{\mathrm{s}}}$), the axial ratio ($q_{\mathrm{s}} = b_{\mathrm{s}}/a_{\mathrm{s}}$), and the position angle (ϕ_{s}). The total number of free parameters is $N_{\mathrm{free}} = 14$. The best-fit model is obtained by maximizing the Gaussian likelihood function $\mathcal{L}$ according to:

$$\mathcal{L} = \sum_{u,v} \left(\frac{|V_{\mathrm{data}} - V_{\mathrm{model}}|^2}{\sigma^2} + \log(2\pi\sigma^2) \right) \quad (1)$$

where σ is determined from the scatter in the visibilities within a single spectral window ("natural" weighting).

We initialize the positions and Einstein radii of both lenses, and the position of the source using the best-fit values of the lens model H14 performed on Keck K-band (near-infrared) data. For each of these parameters, we impose a uniform prior in the range $\in \pm 3\sigma$, where σ is the uncertainty reported in their paper. The axial ratios of the lenses are restricted to $q_{\mathrm{lens}} > 0.3$. We initialize 512 walkers and 6000 steps to identify the best-fit model parameters.

The resulting best-fit model as shown in Figure 3

TABLE 1
LENS MODELING RESULTS

Parameters		Best-Fit Values
Lens 0		
$\Delta\alpha_{\mathrm{lens0}}$	$('')$	0.403 ± 0.026
$\Delta\delta_{\mathrm{lens0}}$	$('')$	-0.181 ± 0.027
q_{lens0} [a]		0.446 ± 0.063
ϕ_{lens0}	(deg)	31.56 ± 4.15
θ_{E0}	$('')$	1.218 ± 0.010
Lens 1		
$\Delta\alpha_{\mathrm{lens1}}$	$('')$	-0.804 ± 0.034
$\Delta\delta_{\mathrm{lens1}}$	$('')$	-1.243 ± 0.017
q_{lens1} [a]		0.608 ± 0.138
ϕ_{lens1}	(deg)	14.2 ± 15.7
θ_{E1}	$('')$	0.745 ± 0.015
Source		
$\Delta\alpha_{\mathrm{s}}$	$('')$	-0.163 ± 0.035
$\Delta\delta_{\mathrm{s}}$	$('')$	-0.193 ± 0.048
q_{s} [a]		0.424 ± 0.237
ϕ_{s}	(deg)	174.34 ± 8.89
r [b]	$('')$	0.106 ± 0.033
μ		10.13 ± 1.38

NOTE. — The angular offsets listed above are with respect to $\alpha = 9{:}39{:}23.54$, $\delta = 83{:}15{:}26.10$ (J2000).

[a] Axial ratio
[b] Effective Radius

shows no significant bowls in the residual image, and the knots (lensed emission) in the observed SMA data are well-reassembled with the best-fit model. Our best-fit model yields a magnification factor of $\mu_{\mathrm{L}} = 10.13 \pm 1.38$, this is consistent the value reported by H14 within the errors. All best-fit parameters are listed in Table 1. The Einstein radii associated with the best-fit model for the two lenses are $\theta_E = 1.22 \pm 0.01$ (8.75 kpc at $z = 0.685$) and $\theta_E = 0.75 \pm 0.02$ (5.34 kpc at $z = 0.685$), the corresponding masses within the Einstein radii are $M(\theta < \theta_{\mathrm{E}}) = (4.86 \pm 0.08) \times 10^{11} \, M_\odot$ and $M(\theta < \theta_{\mathrm{E}}) = (1.82 \pm 0.07) \times 10^{11} \, M_\odot$, respectively.

4.2. SED Fitting
4.2.1. 3C220.3

Synchrotron continuum emission from extended components of a radio galaxy decreases with increasing radio frequencies, and the spectrum is commonly characterized by a power law distribution $S \propto \nu^{-\alpha}$, where the spectral index α is $\gtrsim 0.5$. While the contribution from extended components decreases, studies using samples of radio galaxies have suggested that the flat/inverted-spectrum of the compact radio core component rises and dominates the flux density at higher frequencies (Kellermann & Pauliny-Toth 1981; Begelman et al. 1984). This has been observed in a FR-II galaxy at a similar redshift – 3C220.1 at the redshift of $z = 0.610$, where observations were carried out at observed-frame ~ 90 GHz (Hardcastle & Looney 2008). It is noteworthy that prior to our observations, 3C220.1 was the only FR-II galaxy with high frequency observations at $z > 0.6$. Previous studies of the core component of 3C220.3 have established upper limit of < 0.17 mJy at 4.6 GHz (Mullin et al. 2006) and

TABLE 2
CONTINUUM DATA OF 3C220.3

Frequency		Flux Density		Ref.
104.2	GHz	7.50 ± 1.30 [a]	mJy	This work
10.7	GHz	270 ± 30	mJy	K73
10.7	GHz	253 ± 28	mJy	L80
9.0	GHz	0.80 ± 0.06 [b]	mJy	H14
5.0	GHz	640 ± 100	mJy	K69
5.0	GHz	636 ± 50	mJy	L80
4.86	GHz	< 0.17 [b]	mJy	M06
2.7	GHz	1.33 ± 0.07	Jy	K69
2.7	GHz	1.34 ± 0.10	Jy	L80
1.4	GHz	2.95 ± 0.09	Jy	C98
1.4	GHz	2.99 ± 0.06	Jy	P66
1.4	GHz	2.80 ± 0.14	Jy	K69
1.4	GHz	2.89 ± 0.09	Jy	L80
0.75	GHz	5.94 ± 0.28	Jy	L80
0.75	GHz	5.94 ± 0.21	Jy	P66
0.75	GHz	5.60 ± 0.84	Jy	K69
352	MHz	11.3 ± 0.453	Jy	WENSS
352	MHz	11.6 ± 0.464	Jy	WENSS
178	MHz	15.7 ± 2.35	Jy	K69
178	MHz	17.1 ± 1.71	Jy	L80
152	MHz	22.6 ± 0.08	Jy	B85
152	MHz	22.5 ± 0.04	Jy	B85
86	MHz	51.6 ± 9.90	Jy	L80
73.8	MHz	37.5 ± 3.82	Jy	C07
38	MHz	49.6 ± 4.96	Jy	L80
38	MHz	40.2 ± 6.30	Jy	K69
37.8	MHz	60.7 ± 6.07	Jy	H95
17.8	MHz	64.9 ± 6.49	Jy	H95

NOTE. — References. K93 = Kellermann & Pauliny-Toth (1973); L80 = Laing & Peacock (1980); K69 = Kellermann et al. (1969); H14 = Haas et al. (2014); M06 = Mullin et al. (2006); C98 = Condon et al. (1998); P66 = Pauliny-Toth et al. (1966); B85 = Baldwin et al. (1985); C07 = Cohen et al. (2007); H95 = Hales et al. (1995); WENSS = Rengelink et al. (1997) [c]

[a] This value is the integrated flux density. The peak flux density at the peak position of the continuum emission is 4.91 ± 0.54 mJy

[b] Core

[c] www.astron.nl/wow/testcode.php?survey=1

an unambiguous detection of 0.8 mJy at 9 GHz (H14), suggesting a substantially inverted spectrum of the core (Figure 4). Consequently, we may naively expect the integrated flux density in our continuum detection of $S_{104\mathrm{GHz}} = 7.50 \pm 1.30$ mJy to be dominated by the unresolved core component of the foreground FR-II galaxy, which is at $z = 0.685$. However, the inferred deconvolved spatial size of the source matching that in the resolved image (see Figure 1) is suggestive of a marginally resolved detection of the extended components with non-negligible emission. This is plausible given that the orientation of the synthesized beam in our observations is in alignment with the axis along the lobes of the radio galaxy, as shown in Figure 1. We investigate this disparity by fitting models to existing SED data of the total integrated flux as listed in Table 2, and extrapolating the fit to estimate the flux density of the lobes at the frequency of our continuum measurement.

Following Equation (1) in Cleary et al. (2007), the fit to the lobe emission can be expressed as a parabolic function:

$$\log F_\nu^{lobe}(\nu) \propto -\beta (\log \nu - \log \nu_t)^2 + \log(\exp(\frac{\nu}{\nu_c^{lobe}})) \quad (2)$$

where F_ν^{lobe} is the flux density of the lobes, β is a param-

eter representing the bending of the parabola, ν_t is the frequency at which the optical depth of the synchrotron emitting plasma reaches unity, and ν_c^{lobe} is the frequency corresponding to the cutoff energy of the lobe plasma energy distribution. The extrapolated flux density at 104 GHz is consistent with the flux density of our continuum measurement (Figure 4). The 9σ detection of the continuum thereby suggests a dominant contribution from the lobes, and the peak flux density therefore does not appear to be emission toward the core. Moreover, the peak position of the 104 GHz continuum is centered toward the northern lobe (Figure 1), which further supports our argument. We did not extrapolate the core measurements to the frequency of our continuum, as previous measurements of the core are taken across different epochs. EDIT HERE

From our interpretation, we place an upper limit of $S_\nu < 2.59$ mJy on the core component using the difference.

Studies by Meisenheimer et al. (1989) and Hardcastle & Looney (2008) have suggested spectra of hotspots are flat up to optical frequencies, where some exhibit spectral steepening in cm and mm wavelengths (e.g., 3C123). At the resolution of our observations, it is unclear whether the integrated flux is dominated by the emission from the compact hotspot or the emission from the surrounding diffuse lobe components.
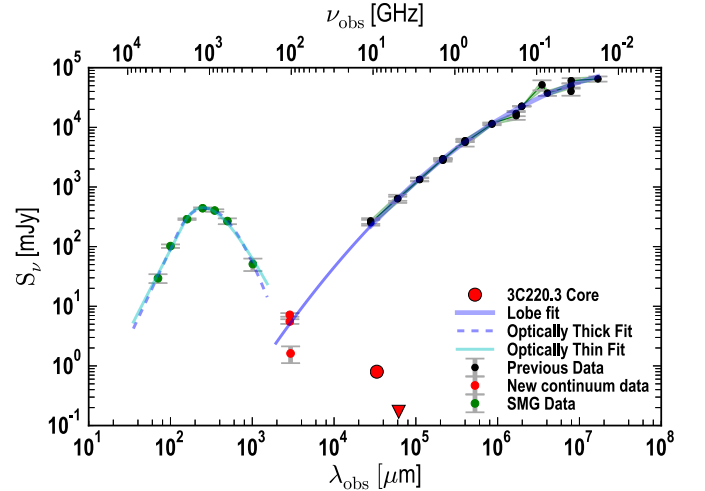

FIG. 4.— The SED of 3C220.3 (solid purple line) and SMM J0939 (dashed purple line and solid cyan line) including the new measurements presented in this paper. Black dots represent existing data of 3C220.3 (see Table 2). Red dots at 104 GHz correspond to our continuum measurements (integrated, peak, and difference). The purple line corresponds to the parabolic function we fit to the data associated with the radio galaxy, following Cleary et al. (2007). The dashed purple line and the solid cyan line correspond to the best-fit SED models of the background SMG. The photometric data of the SMG are reported by H14.

4.2.2. SMM J0939+8315

To constrain the dust and gas properties in the ISM of SMM J0939, we perform SED fitting to the photometric data obtained with *Herschel*/PACS and SPIRE, at wavelengths between observed-frame 70 μm− 500 μm, and interferometric data with the SMA at 1 mm (H14).

TABLE 3
SED fitting results

Parameters	Optically Thick	Optically Thin
χ^2	2.25	5.31
D.O.F	2	3
T	$63.1^{+1.1}_{-1.3}$	$52.0^{+1.3}_{-1.2}$
β	$1.90^{+0.6}_{-0.5}$	$0.7^{+0.2}_{-0.3}$
α	$2.9^{+0.3}_{-0.4}$	$2.8^{+0.2}_{-0.2}$
λ_0 [a]	$248.7^{+86.0}_{-123.8}$	—
$\lambda_{\rm peak}$ [b]	$254.7^{+6.2}_{-6.1}$	$301.4^{+29.0}_{-30.1}$
$f_{\rm norm,\,500\mu m}$ [c]	$267.4^{+16.7}_{-16.3}$	$244.3^{+15.3}_{-15.3}$
$L_{\rm IR}$ [d]	$88.5^{+2.6}_{-2.6}$	$89.2^{+2.5}_{-2.5}$
$M_{\rm d}$ [e]	$50.5^{+20.4}_{-20.2}$	$25.7^{+3.9}_{-5.5}$

NOTE. — Errors reported here are $\pm 1\sigma$. $L_{\rm IR}$ and $M_{\rm d}$ are prior to lensing correction.
[a] The rest-frame wavelength in units of μm where the dust becomes optically thick, upper limit is 2000 μm
[b] Observed-frame wavelength in units of μm
[c] Observed-frame flux density at 500 μm
[d] Rest-frame 8-1000 μm luminosity in units of 10^{12} $L_\odot$
[e] Dust mass in units of 10^8 $M_\odot$, derived assuming standard absorption mass coefficient κ=2.64 m^2 kg^{-1} at λ=125.0 μm (Dunne et al. 2003), without lensing correction

We use the publicly available software MBB_EMCEE[3] to perform the SED fitting; the code uses an affine-invariant Markov chain Monte Carlo (MCMC) approach, and further details of the code are given by Riechers et al. (2013) and Dowell et al. (2014). The functional form of the fit comprises a single-temperature, modified blackbody function joined to a $S_\lambda \propto \lambda^\alpha$ power law on the blue side of the SED. We fit both optically thick and optically thin models. In the optically thick case, the wavelength $\lambda_0 = c/\nu_0$ is an additional parameter representing the rest-frame wavelength at which the optical depth $\tau_\nu = (\nu/\nu_0)^\beta$ reaches unity. Thus, the functional form of the modified blackbody in the optically thick regime is as follows:

$$S_\lambda \propto \frac{(1 - \exp^{-(\frac{\lambda_0(1+z)}{\lambda})^\beta})(\frac{c}{\lambda})^3}{\exp^{\frac{hc}{\lambda kT/(1+z)}} - 1} \quad (3)$$

and in the optically thin regime, the functional form reduces to:

$$S_\lambda \propto \frac{(\frac{c}{\lambda})^{\beta+3}}{\exp^{\frac{hc}{\lambda kT/(1+z)}} - 1} \quad (4)$$

where T is the rest-frame characteristic cold dust temperature, β is the dust emissivity (or spectral index of the dust extinction curve), and α is the power law spectral index. The overall fit is normalized using the observed-frame 500 μm flux density, hence this becomes an additional parameter in the fit. For both models, we impose an upper limit on the observed-frame dust temperature $(T/(1+z))$ to 60 K, and for the optically thick model, we impose an upper limit on λ_0 to 2000 μm. Additionally, we fix the upper limits on β to be 3.0 and 2.2 for the optically thin model and optically thick model, respectively.

The best-fit values in both regimes are listed in Table 3, and the correlation plots are available in the Appendix.

[3] https://github.com/aconley/mbb_emcee

The best-fit solution of an optically thin model corresponds to $\chi^2 = 5.31$ with 3 degrees of freedom, whereas that of an optically thick model corresponds to $\chi^2 = 2.25$ with 2 degrees of freedom, suggesting a better fit than in the optically thin case. In the subsequent analysis, we employ the inferred values from the optically thick model. The best-fit solution yields a rest-frame FIR luminosity of $L_{\rm FIR(42.5-122.5\mu m)} = 53.3^{+1.1}_{-1.1} \times 10^{12} L_\odot$, and a total infrared (IR) luminosity of $L_{\rm IR(8-1000\mu m)} = 88.5^{+2.6}_{-2.6} \times 10^{12} L_\odot$. Assuming a dust absorption coefficient of $\kappa_\nu = 2.64$ m^2 kg^{-1} at 125.0 μm (Dunne et al. 2003), we derive the dust mass using the following expression:

$$M_{\rm dust} = S_\nu D_L^2 [(1+z)\kappa_\nu B_\nu]^{-1} \tau_\nu [1 - \exp(-\tau_\nu)]^{-1} \quad (5)$$

where S_ν is the flux density in ergs/s/cm^2/Hz , $D_{\rm L}$ is the luminosity distance in cm, κ_ν is the dust absorption coefficient in cm^2 g^{-1}, τ_ν is the optical depth, and B_ν is the Planck function, all quantities are expressed in the observed-frame. We find a dust mass of $M_{\rm dust} = 50.5^{20.4}_{-20.2} \times 10^8$ $M_\odot$, the uncertainties do not include those of κ_ν. These values are based on SED fitting to the photometric data, i.e., prior to lensing correction.

With the limited amount of data in the FIR waveband, the dust mass is weakly constrained. We perform an additional SED fitting using an optically thick model where we loosen the upper limit of β from 2.2 to 3.0, while the difference between all best-fit parameters in this scenario and those using an upper limit of 2.2 (see Table 3) is within 3%, we find that the dust mass is boosted by a factor of ~ 2.

4.3. Molecular Gas Mass

While the ground state CO transition line, CO($J = 1 \rightarrow 0$) traces the cold molecular gas in the ISM (e.g., Downes & Solomon 1998; Wilson, Jefferts, & Penzias 1970), CO($J > 1$) transition lines are frequently observed at high redshifts as the ground state CO transition line is redshifted to lower frequencies that can only be observed with a few telescopes (Carilli & Walter 2013), hence assumptions on the CO excitation conditions are required to derive the molecular gas mass using the H$_2$-to-CO relation. Prior to the observations of the ground state CO line in SMGs, it has been assumed that the molecular gas in the ISM traced by CO lines is thermalized due to their high star formation rates (e.g., Greve et al. 2005; Coppin et al. 2008). Yet, recent observations of this line have demonstrated that SMGs can indeed be subthermally excited (Harris et al. 2010; Riechers et al. 2011a,b; Ivison et al. 2011); based on observations toward SMGs of both the CO($J = 3 \rightarrow 2$) and the CO($J = 1 \rightarrow 0$) lines, the brightness temperature ratio has been inferred as $R_{31} < 0.8$ (Harris et al. 2010; Carilli et al. 2010; Swinbank et al. 2010; Riechers et al. 2011b; Ivison et al. 2011, 2010a). In contrast, observations of high-redshift quasar hosts suggest that the ratio is $R_{31} \sim 1$ (Riechers et al. 2006, 2011c; Scott et al. 2011). Here, we derive the molecular gas mass assuming thermalized excitation of CO, e.g., we adopt $R_{31} = 1$ as SMM J0939 is postulated to be hosting a type-2 quasar; this is based on the reported brightness temperature ratio of $R_{31} = 1.00 \pm 0.10$ for the type-2 quasar host IRAS F10214+4724 (Riechers et al. 2011c).

We calculate the CO($J = 1 \rightarrow 0$) line luminosity using standard relation (*e.g.,* Solomon & Vanden Bout 2005; Carilli & Walter 2013):

$$L'_{\rm CO} = \frac{3.25 \times 10^7}{\nu^2_{\rm CO(3-2),rest}} \times \frac{D_L^2}{\mu} \times \frac{I_{\rm CO(3-2)}}{R_{31}(1+z)} \qquad (6)$$

where $\nu_{\rm CO(3-2),rest}$ is the rest-frame frequency of the CO($J = 3 \rightarrow 2$) line in GHz, D_L is the luminosity distance in Mpc, and $I_{\rm CO(3-2)}$ is the CO($J = 3 \rightarrow 2$) line flux in Jy km s^{-1}. This corresponds to $L'_{\rm CO(1-0)} = (2.91 \pm 0.78) \times 10^{10} (10.1/\mu_{\rm L})$ K km s^{-1} pc^2 after correcting for lensing magnification; the inferred total molecular gas mass is therefore $M_{\rm gas} = (2.33 \pm 0.62) \times 10^{10} M_\odot$. We assumed a conversion factor of $\alpha_{\rm CO} = 0.8$ $M_\odot$(K km s^{-1} pc^2)$^{-1}$ based on empirical relations from local ULIRGs, which is typically adopted for SMGs (*e.g.,* Tacconi et al. 2006, 2008; Bothwell et al. 2013). This results in a gas-to-dust ratio of $f_{\rm gas-dust} = M_{\rm gas}/M_{\rm dust} = 47 \pm 21$, this is in good agreement with the values found in other SMGs (Coppin et al. 2008; Michałowski et al. 2010; Riechers et al. 2011a).

4.4. *Star Formation Rate*

No strong evidence of a warm dust component is found in SMM J0939 based on the mid-IR continuum measurements (see Figure 4), hence we derive the star formation rate (SFR) assuming negligible contributions to the IR luminosity due to AGN heating. Using the Kennicutt (1998) relation and assuming Chabrier (2003) stellar initial mass (IMF) function[4], the SFR$_{\rm IR}$ is 874 ± 122 $M_\odot$ yr^{-1}. Assuming constant SFR, the time for which the starburst in SMM J0939 can be maintained at its current SFR can be approximated as the gas depletion timescale, $\tau_{\rm depl} = M_{\rm gas}/{\rm SFR}$. This corresponds to $\tau_{\rm depl} = 25.6 \pm 0.6$ Myr, which is in good agreement with that found in other SMGs (*e.g.,* Greve et al. 2005).

4.5. *Star Formation Efficiency*

The SFR per unit mass of molecular gas is commonly taken as a measure of the star formation efficiency, SFE $= $ SFR$/M_{\rm gas}$. We compute this ratio using lensing-corrected IR luminosity and CO luminosity, i.e., SFE $= L_{\rm IR}/L'_{\rm CO(1-0)}$, this makes no assumptions on the CO luminosity to gas mass conversion factor ($\alpha_{\rm CO}$) as well as the choice of IMF, however, this assumes that differential lensing effect between the CO and infrared emission is negligible. The resulting ratio is SFE$_{\rm IR} = 300 \pm 10$ L$_\odot$(K km s^{-1} pc^2)$^{-1}$, this is comparable to what is found in "typical" SMGs (Riechers et al. 2011a; Tacconi et al. 2006; Greve et al. 2005).

4.6. *Dynamical Mass*

Based on our CO($J = 3 \rightarrow 2$) line measurement, we can estimate the dynamical mass of SMM J0939 using an isotropic virial estimator (*e.g.,* Engel et al. 2010):

$$M_{\rm dyn} = 2.8 \times 10^5 \Delta v_{\rm line}^2 R_{\rm eff} \qquad (7)$$

[4] SFR$_{\rm FIR} = 526 \pm 72$ $M_\odot$ yr^{-1}

where $\Delta v_{\rm line}$ is in km s^{-1}, $R_{\rm eff}$ is in kpc, and $M_{\rm dyn}$ is in $M_\odot$. We employ the FWHM linewidth of the CO($J = 3 \rightarrow 2$) line for $\Delta v_{\rm line}$, and the half-light radius from our lens model for $R_{\rm eff}$, this assumes that the dust emission traces the same emitting region as the CO. The inferred dynamical mass is $M_{\rm dyn} = (7.4 \pm 2.4) \times 10^{10} M_\odot$, and the gas-to-dynamical mass fraction is $f_{\rm gas-to-dyn} = 0.32 \pm 0.14$, this is consistent with that of other SMGs (Tacconi et al. 2006).

4.7. *Star Formation and Gas Surface Densities*

To compute surface densities, we divided half the inferred SFR and gas mass by the area subtended by the half-light radius, resulting in $\Sigma_{\rm gas} = 4.67 \times 10^9$ $M_\odot$ kpc^{-2} and $\Sigma_{\rm SF} = 175.20$ $M_\odot$ yr^{-1} kpc^{-2}, in good agreement with values typical for SMGs (Tacconi et al. 2008).

The inferred surface densities of SMM J0939 follow a universal Schmidt-Kennicutt relation between the star formation rate surface density and the molecular gas surface density reported by Bouché et al. (2007): $\Sigma_{\rm SF} = 9.3 \times 10^{-5} (M_{\rm gas}/2\pi R_{1/2}^2)^{1.71}$, which was derived using a sample consisting of high-redshift galaxies and local star-forming galaxies out to $z \sim 2.5$, and assuming Chabrier IMF.

5. DISCUSSION AND CONCLUSIONS

We present the detection of CO($J = 3 \rightarrow 2$) line emission toward SMM J0939+8315, a strongly lensed SMG that is hosting a type-2 quasar, confirming the redshift of SMM J0939 with high precision at $z = 2.22122 \pm 0.00007$. The peculiarity of this system allows us to put constraints on the SED of 3C220.3 using the underlying continuum detection at $\sim$104 GHz, we argue that the result is suggestive of a dominant contribution from the lobes and hotspots.

The detection of CO with CO luminosity of $L'_{\rm CO(1-0)} = $ blah K km s^{-1} pc^2 in SMM J0939 implies the presence of a large molecular gas reservoir, demonstrating the active star formation in this SMG with SFR $\sim$ 874 $M_\odot$ yr^{-1}. Our findings are typical for SMGs, which supports the picture that SMGs are a population of high-z galaxies that spawn most of the stellar mass in the early universe, thus play an important role in galaxy evolution and formation.

The detection of thermal dust emission in SMM J0939 implies a FIR Luminosity of Assuming the dominant heating mechanism is from young, massive stars, then the SFR implied from the LIR is blah From the IR continuum data, we expected contribution to the bolometric IR luminosity due to heating of the dust-enshrouded AGN is minor, the physical properties are therefore derived using the lensing-corrected bolometric IR luminosity. The high dust temperature is unusual for SMGs, but not unseen.

We compare the properties of SMM J0939 with those found in strongly lensed, submm-bright galaxies at similar redshift – HLSW-01 and the cosmic Eyelash, which have been studied in great detail. We list the gas and dust properties of these galaxies in Table 4,

Discussion of SMG, broad, population. We compare the properties of SMM J0939 to a type-2 quasar host – F10214+2724, in which the molecular gas has been studied in great detail (Riechers et al. 2011c).

TABLE 4
COMPARISON OF SMM J0939 WITH SMGs AT $z \sim 2$

Quantity	SMGs Unit	SMM J0939	HLSW-01	Ref.	Cosmic Eyelash	Ref.
z		2.221	2.957	R11	2.326	S10
$\mu_{\rm L}$		10.1 ± 1.4	10.9 ± 0.7	G11	37.5 ± 4.5	S11
S_{250}	mJy	440 ± 15 [a]	425 ± 10	C11	366 ± 55	I10
I [b]	Jy km s^{-1}	10.7 ± 1.3	9.7 ± 0.5	R11	13.2 ± 0.1	D11
$\Delta v_{\rm FWHM}$ [b]	km s^{-1}	557 ± 36	350 ± 25	R11	$\lesssim 800$ [c]	D11
$L'_{\rm CO(1-0)}$	10^{10} K km s^{-1} pc^2	2.9 ± 0.8 [e]	4.2 ± 0.4	R11	1.7 ± 0.2	D11
$M_{\rm gas}$	10^{10} $M_\odot$	2.3 ± 0.6 [e]	3.3 ± 0.3	R11	1.6 ± 0.1	I10
$L_{\rm IR}$	10^{12} L$_\odot$	9.1 ± 1.2 [e]	14.3 ± 0.9	C11	2.3 ± 0.2	I10
$M_{\rm dust}$	10^8 $M_\odot$	5.2 ± 2.1 [e]	$1 - 5.2$	R11	~ 4.0	I10
SFR$_{\rm IR}$ [d]	$M_\odot$yr^{-1}	874 ± 122 [e]	1430 ± 160 [g]	C11	~ 235 [g]	I10
$\tau_{\rm depl}$ [h]	Myr	25.6 ± 0.6	23 ± 3 [g]	R11	68 [f]	—
$f_{\rm gas-dust}$ [h]		47 ± 21	$60 - 330$	R11	~ 40	I10
SFE [h]	L$_\odot$ (K km s^{-1} pc^2)$^{-1}$	300 ± 10	340 ± 40	R11	135 ± 20 [f]	—
$M_{\rm dyn}$ [h]	10^{10} $M_\odot$	7.4 ± 2.4	3.7 ± 1.8 [f i]	—	6.0 ± 0.5	S11
$f_{\rm gas-dyn}$		0.3 ± 0.1	0.9 [f i]	—	0.6 ± 0.1	S11

NOTE. — Values listed from rows 6 onwards are lensing-corrected. References. C11 = Conley et al. (2011); D11 = Danielson et al. (2011); G11 = Gavazzi et al. (2011); I10 = Ivison et al. (2010b); R11 = Riechers et al. (2011d); S11 = Swinbank et al. (2011); S10 = Swinbank et al. (2010)
[a] H14
[b] CO($J = 3 \to 2$)
[c] Estimated from Figure 1 in D11
[d] Chabrier IMF
[e] Errors include uncertainties on $\mu_{\rm L}$
[f] We derive this using the reported values
[g] Converted theirs values derived using Salpeter IMF to Chabrier IMF
[h] Independent of lensing magnification factor $\mu_{\rm L}$
[i] Using CO($J = 5 \to 4$)

REFERENCES

Baldwin, J. E., Boysen, R. C., Hales, S. E. G., et al. 1985, MNRAS, 217, 717
Begelman, M. C., Blandford, R. D., & Rees, M. J. 1984, Reviews of Modern Physics, 56, 255
Blain, A. W., Smail, I., Ivison, R. J., Kneib, J.-P., & Frayer, D. T. 2002, Phys. Rep., 369, 111
Bothwell, M. S., Smail, I., Chapman, S. C., et al. 2013, MNRAS, 429, 3047
Bouché, N., Cresci, G., Davies, R., et al. 2007, ApJ, 671, 303
Bussmann, R. S., Riechers, D., Fialkov, A., et al. 2015, ArXiv e-prints, arXiv:1504.05256
Carilli, C. L., & Walter, F. 2013, ARA&A, 51, 105
Carilli, C. L., Daddi, E., Riechers, D., et al. 2010, ApJ, 714, 1407
Chabrier, G. 2003, PASP, 115, 763
Cleary, K., Lawrence, C. R., Marshall, J. A., Hao, L., & Meier, D. 2007, ApJ, 660, 117
Cohen, A. S., Lane, W. M., Cotton, W. D., et al. 2007, AJ, 134, 1245
Condon, J. J., Cotton, W. D., Greisen, E. W., et al. 1998, AJ, 115, 1693
Conley, A., Cooray, A., Vieira, J. D., et al. 2011, ApJ, 732, L35
Coppin, K. E. K., Swinbank, A. M., Neri, R., et al. 2008, MNRAS, 389, 45
Danielson, A. L. R., Swinbank, A. M., Smail, I., et al. 2011, MNRAS, 410, 1687
Dowell, C. D., Conley, A., Glenn, J., et al. 2014, ApJ, 780, 75
Downes, D., & Solomon, P. M. 1998, ApJ, 507, 615
Dunne, L., Eales, S. A., & Edmunds, M. G. 2003, MNRAS, 341, 589
Eales, S., Dunne, L., Clements, D., et al. 2010, PASP, 122, 499
Engel, H., Tacconi, L. J., Davies, R. I., et al. 2010, ApJ, 724, 233
Fanaroff, B. L., & Riley, J. M. 1974, MNRAS, 167, 31P
Gavazzi, R., Cooray, A., Conley, A., et al. 2011, ApJ, 738, 125
Greve, T. R., Bertoldi, F., Smail, I., et al. 2005, MNRAS, 359, 1165

Haas, M., Leipski, C., Barthel, P., et al. 2014, ApJ, 790, 46 (H14)
Hales, S. E. G., Waldram, E. M., Rees, N., & Warner, P. J. 1995, MNRAS, 274, 447
Hardcastle, M. J., & Looney, L. W. 2008, MNRAS, 388, 176
Harris, A. I., Baker, A. J., Zonak, S. G., et al. 2010, ApJ, 723, 1139
Hinshaw, G., Larson, D., Komatsu, E., et al. 2013, ApJS, 208, 19
Ivison, R. J., Papadopoulos, P. P., Smail, I., et al. 2011, MNRAS, 412, 1913
Ivison, R. J., Smail, I., Papadopoulos, P. P., et al. 2010a, MNRAS, 404, 198
Ivison, R. J., Swinbank, A. M., Swinyard, B., et al. 2010b, A&A, 518, L35
Kellermann, K. I., & Pauliny-Toth, I. I. K. 1973, AJ, 78, 828
—. 1981, ARA&A, 19, 373
Kellermann, K. I., Pauliny-Toth, I. I. K., & Williams, P. J. S. 1969, ApJ, 157, 1
Kennicutt, Jr., R. C. 1998, ARA&A, 36, 189
Lagache, G., Puget, J.-L., & Dole, H. 2005, ARA&A, 43, 727
Laing, R. A., & Peacock, J. A. 1980, MNRAS, 190, 903
Meisenheimer, K., Roser, H.-J., Hiltner, P. R., et al. 1989, A&A, 219, 63
Michałowski, M. J., Watson, D., & Hjorth, J. 2010, ApJ, 712, 942
Mullin, L. M., Hardcastle, M. J., & Riley, J. M. 2006, MNRAS, 372, 113
Negrello, M., Hopwood, R., De Zotti, G., et al. 2010, Science, 330, 800
Oliver, S. J., Bock, J., Altieri, B., et al. 2012, MNRAS, 424, 1614
Pauliny-Toth, I. I. K., Wade, C. M., & Heeschen, D. S. 1966, ApJS, 13, 65
Rengelink, R. B., Tang, Y., de Bruyn, A. G., et al. 1997, A&AS, 124, 259
Riechers, D. A., Walter, F., Carilli, C. L., et al. 2006, ApJ, 650, 604

Riechers, D. A., Hodge, J., Walter, F., Carilli, C. L., & Bertoldi,
    F. 2011a, ApJ, 739, L31
Riechers, D. A., Carilli, L. C., Walter, F., et al. 2011b, ApJ, 733,
    L11
Riechers, D. A., Carilli, C. L., Maddalena, R. J., et al. 2011c,
    ApJ, 739, L32
Riechers, D. A., Cooray, A., Omont, A., et al. 2011d, ApJ, 733,
    L12
Riechers, D. A., Bradford, C. M., Clements, D. L., et al. 2013,
    Nature, 496, 329
Scott, K. S., Lupu, R. E., Aguirre, J. E., et al. 2011, ApJ, 733, 29
Smolčić, V., & Riechers, D. A. 2011, ApJ, 730, 64

Solomon, P. M., & Vanden Bout, P. A. 2005, ARA&A, 43, 677
Swinbank, A. M., Smail, I., Longmore, S., et al. 2010, Nature,
    464, 733
Swinbank, A. M., Papadopoulos, P. P., Cox, P., et al. 2011, ApJ,
    742, 11
Tacconi, L. J., Neri, R., Chapman, S. C., et al. 2006, ApJ, 640,
    228
Tacconi, L. J., Genzel, R., Smail, I., et al. 2008, ApJ, 680, 246
Vieira, J. D., Crawford, T. M., Switzer, E. R., et al. 2010, ApJ,
    719, 763
Wilson, R. W., Jefferts, K. B., & Penzias, A. A. 1970, ApJ, 161,
    L43

APPENDIX

We perform SED fitting to the IR photometric data of SMM J0939 using MBB_EMCEE (see §4.2.2), this code uses MCMC to fully sample the parameter space of each parameter. The bolometric IR luminosity and dust mass are then derived from the set of parameter values that maximize the likelihood. Figure 5 shows the correlations between each pair of parameters (off-diagonal) as well as the marginalized posterior probability distribution of each parameter (diagonal) for both optically thick and optically thin models. The set of best-fit parameters are denoted as black crosses in the 2D correlation plots, and vertical lines in the marginalized posterior probability distribution plots.
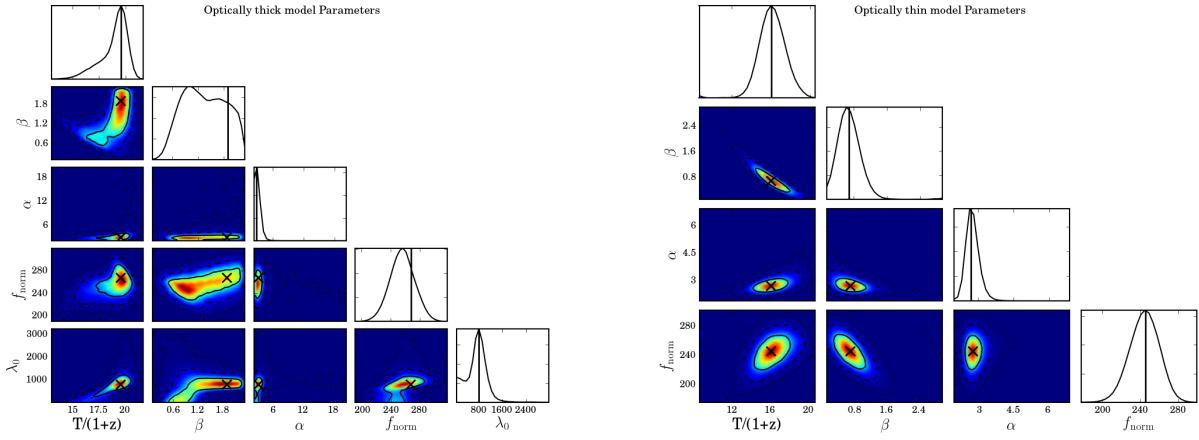

FIG. 5.— Correlation plots from our SED fitting using an optically thick model (left), and an optically thin model (right). Marginalized posterior probability distribution of each parameter is plotted on the diagonal axis of each panel, where the vertical lines indicate the best-fit value. The correlation plots between parameters are plotted as 2D histograms in the off-diagonal. Black crosses on each 2D histogram denote the best-fit values in the 2D correlation plot.